NANO SPHERE SHAPED WO$_3$ ANCHORED ON MWCNT FOR HIGH PERFORMANCE OF ASYMMETRIC SUPER CAPACITORS

M.Kalaivani*   **B Gnanavel ****

*PG & Research Department of Physics, Chikkaiah Naicker College, Erode, Tamilnadu, India.
**PG & Research Department of Physics, Chikkaiah Naicker College, Erode – 638 004, Tamilnadu, India.

Abstract
The creation of effective, sustainable, and long-lasting storage systems has piqued the interest of the scientific community, and electrochemical energy storage devices are one of the primary actors in the continuous technical breakthroughs in the energy area. The current study involves the development of an electrode for ASC that is a multi-walled carbon nanotube (MWCNT)/tungsten trioxide (WO3) hybrid nanostructure. The WO3@MWCNT (1:5) hybrid electrode has a maximum specific capacitance of 610 F g-1 (5 Ag-1) and capacity retention of 94.3% after 10,000 cycles. In comparison, pure WO3 in 1 M LiClO4 electrolyte has a maximum specific capacitance of 155.6 F g-1 (0.43 F cm-2) and a capacity retention of 84.9%. The activated carbon is the negative electrode, the WO$_3$@MWCNT(1:5) is the positive electrode, and the PVA-LiClO4 gel electrolyte self-assemble into an ASC. At 2 mA current, the WO$_3$@MWCNT(1:5)//AC ASC has a specific capacitance of 180 F g-1, and at 631 W kg^{-1} of specific power, it has a specific energy of 25.3Wh kg-1. When compared to other types of capacitors, the ASC has better long-term cycling stability (83% over 10,000 cycles) and greater mechanical flexibility with lower capacitance loss. These astonishing findings show the promise of WO$_3$@MWCNT(1:5) hybrid nanostructures for the development of cutting-edge battery technologies.

Keywords: WO$_3$, ASC, Nanosphere, Battery Technologies.

1. Introduction

Many applications requiring local generation or storage of electric energy also demand electrical energy storage. Supercapacitors bridge the gap between batteries and traditional capacitors by providing power densities that extend several orders of magnitudes. Supercapacitors serve as high-power energy storage devices designed for short-term use. They enable the storage of energy from regenerative braking in fuel cells, hybrid electric, and electric cars. There are also a growing number of applications in telecommunications such as mobile phones and personal entertainment devices.

Transition Metal oxides are the oxides of transition metals that have attracted greater attention in the emerging area of nanotechnology due to their unique properties such as photophysical and electronic. Among the various transition oxides, Tungsten oxide is an oxygen-deficient n-type semiconducting material with a wide band gap that received the greater interaction.WO$_3$ has specific properties such as better surface permeability, high specific surface, high melting temperature, mechanical properties, photoelectrochemical, and high toughness which have been widely used in various fields.

Fe2O3 was extensively used as a negative electrode in ASCs due to its wide application range of high negative potential [16, 17]. Several recent articles have discussed the use of V2O5 as an adverse electrode in neutral electrolytes towards ASCs. [18]. Tungsten trioxide (WO3) garnered significant scientific attention during its initial years with pseudocapacitive properties and also possess high energy density [19-23].Reactions taking place on the electrode's surface frequently involve the transfer of electrons and ions with the substance that is being utilized. The poor electrical conductivity of WO3

Research Paper
Impact Factor: 7.352
Peer Reviewed Monthly Journal
www.ijmdrr.com

IJMDRR
E- ISSN –2395-1885
ISSN -2395-1877

hinders its use in producing high-performance supercapacitors, despite its fascinating properties. A potential solution to this issue is using a hybrid electrode that combines carbonaceous materials, which have high conductivity, with a pseudocapacitive substance like WO3. Electrochemical stability and electrical conductivity would be achieved with this combination. With their high electrical conductivity, huge surface area, extraordinary cycle stability, and good mechanical strength, carbon nanotubes (CNTs) have been widely investigated and exploited in flexible energy storage systems [24-26]. In addition, a one-dimensional network of multi-walled carbon nanotubes (MWCNTs) improves electrical conductivity and increases the electrochemically active surface area. This network also facilitates efficient pathways for both electrons and ions in a hybrid electrode.

The present investigation developed on MWCNTs and WO3 combined into a solitary electrode. The strong affinity between the multi-walled carbon nanotube (MWCNT) structure and the WO3 nanorods led to a notable increase in electrochemical performance.The WO3@MWCNT electrode was utilized as the cathode in an ASC(asymmetric supercapacitor) device, while Activated carbon was employed as the anode. The AC// MWCNT-WO3 ASC device showed that the energy density of the ASC device can be increased in the PVA/LiClO4 gel electrolyte.

2. Materials and Methods
2.1 Methods
Hydrothermal Synthesis is used for synthesizing the tungsten oxide nanoparticles.0.6g of sodium tungstate (Sigma Aldrich) is dissolved in 10ml of distilled water and stirred for 10 minutes at room temperature. Further, 3M of HCl (Sigma Aldrich) is added dropwise to the above solution and maintained the pH values of 7. The above solution turned into milky while attaining the pH value. The obtained solution is transferred to Teflon and heated in the oven at 160°C for 12 hrs. The resulting white precipitate is subjected to centrifugation and dried at 80°C for 6 hrs. To prepare the WO$_3$@MWCNTs nanocomposites, MWCNTs with the ratio of 1:1 and 1:3 is mixed with the tungsten oxide. The mixture is stirred and ultra-sonicated for 2 hours and heated in the oven at 160°C for 10 hrs. The resultant white precipitate is dried at 80°C for 6 hrs.
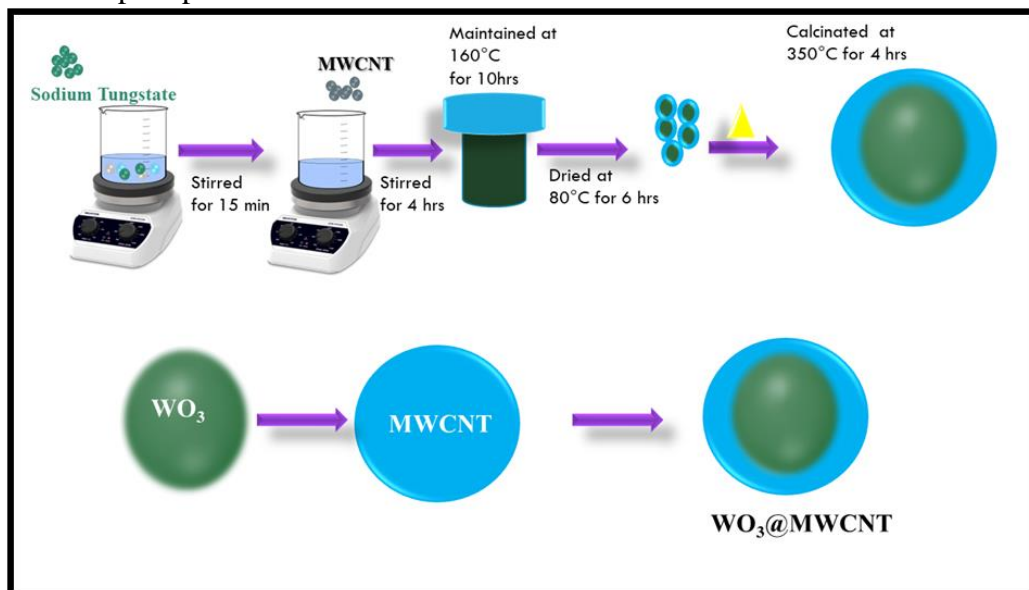

Figure 1. Preparation of WO$_3$@MWCNT (1:1) and WO$_3$@MWCNT (1:5)

2.2 Characterization of Material

The surface patterns of the substances that were produced were analysed employing a scanning electron microscope with field emission (FESEM, JEOL-7800F). The materials that were created were studied using a crystallographic technique called X-ray diffraction. This analysis was performed using a device called a diffractometer, which was equipped with a source of X-rays that had a wavelength of 0.15406 nm and was made of copper (Cu). The X-ray photoelectron spectroscopy (XPS) technique was employed with the VG Scientifics ESCALAB250 device to evaluate the chemical composition and oxidation states of the components in the sample.

2.3 Electrochemical Measurements

The perfect cut into a 1 cm^2 area WO_3, and WO_3@MWCNT electrodes on CC substrates were used as working electrodes. The electrochemical properties were assessed in a three-electrode configuration using cyclic voltammetry (CV), galvanostatic charge-discharge (GCD), and electrochemical impedance (EIS) methods, with a 1 M LiClO4 electrolyte. The reference electrode used in the experiment was a saturated calomel electrode (SCE), and the counter electrode was a platinum wire. The electrochemical test data was analyzed using a ZIVE MP1 electrochemical analyser.

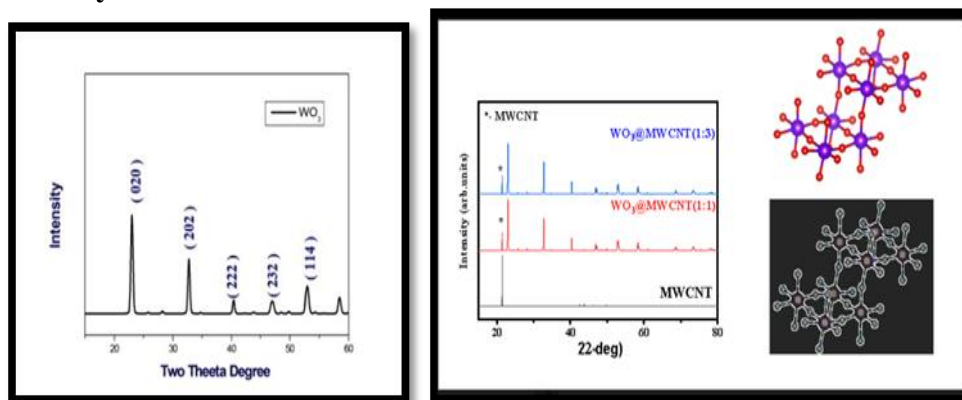## 3. Results and Discussion
3.1 XRD Analysis

Figure 2. XRD analysis of (a) WO$_3$ nanoparticles (b) pure MWCNT, WO$_3$@MWCNT(1:1), WO$_3$@MWCNT (1:3)

The XRD spectrum of WO_3 is shown in Figure 2(a). It is observed from Figure 1(a)that the distinct peaks located at 2Θ values of 23.4°, 33.1°, 41.6°, 49.8° and 50.4° corresponding to the hkl planes at (020),(202),(222),(232) and (114) respectively and have monoclinic structure. The peaks are well indexed with reference to the JCPDS card no (83-0950). Furthermore, Figure 2(b) confirms the pure MWCNT nanoparticles by the presence of carbon peak located at 2Θ values of 22.4° which corresponds to the hkl planes at (002). It is also observed from Figure 1 (b) that tungsten oxide decorated with MWCNT using different concentrations as WO_3@MWCNT (1:1) and WO_3@MWCNT (1:3). The peaks of the WO_3@MWCNT (1:1) and WO_3@MWCNT (1:3) corresponds to (020), (202),(222),(232),(114) and (002) reflects the presence of both $WO_3$and carbon. Furthermore, it is noted that there are no notable disparities in the XRD patterns between pure WO3 and WO3@MWCNT [27] at different concentrations. This can be attributed to the fact that the composite formation with MWCNT preserves the phase purity of WO_3, thereby enhancing its energy storage capability.

Research Paper
Impact Factor: 7.352
Peer Reviewed Monthly Journal
www.ijmdrr.com

IJMDRR
E- ISSN –2395-1885
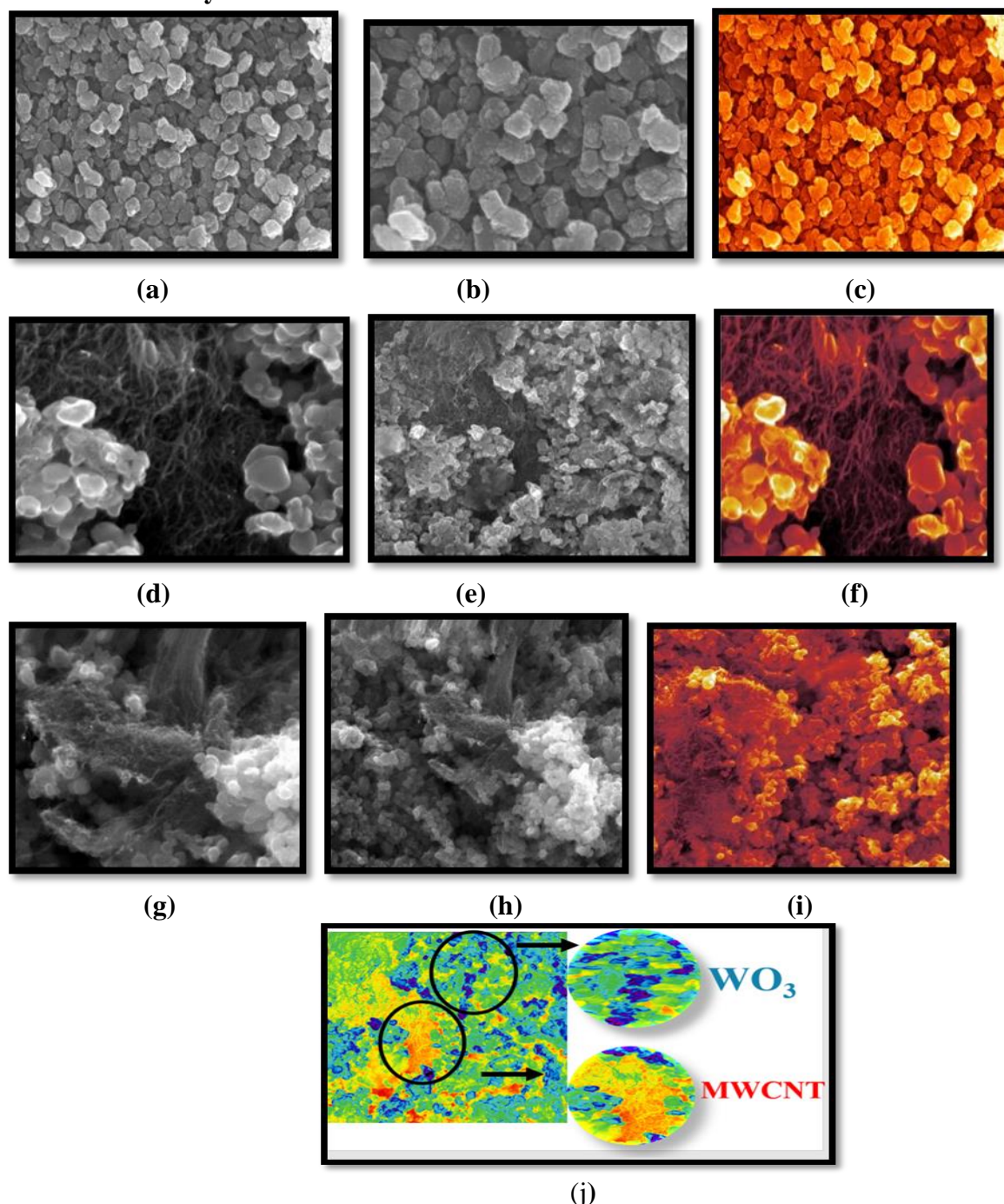*ISSN -2395-1877*

3.2 FESEM Analysis

Figure 3 (a-c) FESEM analysis of pure tungsten oxide (d-f) WO$_3$@MWCNT (1:1) (g-i) WO$_3$@MWCNT (1:5) (j) Simulated FESEM images of MWCNT Coated WO$_3$

Figure.3. (a-i) shows the FESEM analysis of pure tungsten oxide and WO3@MWCNT synthesized using different concentrations (1:1 and 1:5) of MWCNT. The micrographs of pure tungsten oxide show the structure of the spherical shape with a diameter of 25-30 nm. It is also observed from Figure 3. (d-f) MWCNTs are made of interconnected nanospheres into a thread-shaped structure and WO3 with

nanosphere are in the mixed structure in the synthesized nanocomposite using (1:1) concentration. Furthermore, it also observed that the synthesized nanocomposites exhibit homogenous shapes which indicate a strong adhesion between the WO3 and MWCNT. Moreover, the Figure 3. (g-i) shows the WO3@MWCNT (1:5) concentration. By further increase in the concentration of MWCNT on the surface of WO3 is found to be agglomerated, which indicates thereby increasing the cyclic stability of synthesized nanocomposites. Figure 3 (h) displays the simulated images of the prepared samples. Blue areas indicate the presence of WO3 and yellow around the nanosphere of WO3 denotes the presence of MWCNT on the surface of the synthesized nanocomposites.
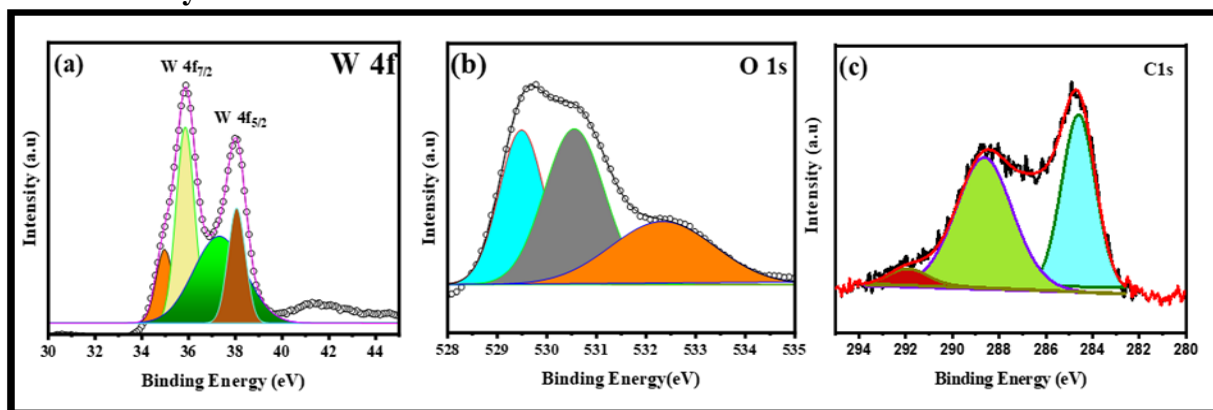
3.3 XPS Analysis

Figure 4 (a-c) XPS analysis of WO$_3$@MWCNT (1:5)

The X-ray photoelectron spectroscopy (XPS) examination was utilised to ascertain the components' oxidation states and chemical structure. Figure 4(b) shows that the W 4f core level spectrum of tungsten in WO3 can be separated into the W 4f5/2 and W 4f7/2 orbitals at 37.75 and 35.58 eV with W6+ oxidation state respectively[28]. The spectra of C 1s (Figure 4(c)) exhibit peaks at 285.1 eV (C–C), 286.5 eV (C–O), and 283.0 eV (C=O)[29]. The spectra of the O 1s (Figure 4(c)) have a prominent peak at 530.8 eV, indicating the presence of metal-oxygen bonding in the lattice (WO). Additionally, there are two peaks observed at 531.6 and 532.5 eV, corresponding to surface groups (OOH) and (CO).
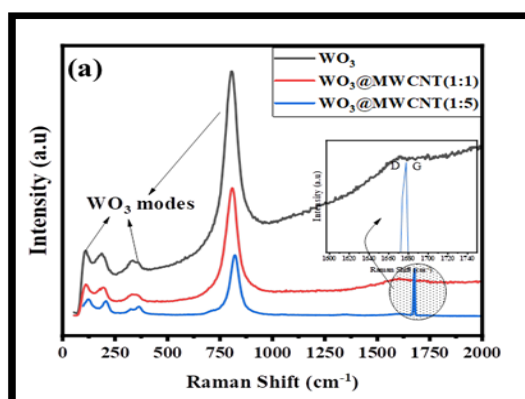
3.4. Raman Analysis

Figure 5 Raman analysis (a) pure WO$_3$ (b) WO$_3$@MWCNT (1:1) (c) WO$_3$@MWCNT (1:5) nanocomposites

Figure 5 (a-c) displays the Raman spectra of WO3 and WO3@MWCNT (1:1 and 1:5) nanocomposites. Figure 5 (a) shows a peak at 807 cm-1, indicating the presence of O-W-O stretching vibration modes of bridging oxygens of WO6. The peaks seen between the range of 190 cm-1 to 270 cm-1 in WO3@MWCNT (1:1 and 1:5) nanocomposites are a result of the stretching, bending, or deformation of O-W-O bonds. Furthermore, Figure 5 (c) illustrates that the MWCNT has two distinct bands, namely the D-band and the G-band, located at 1332 and 1594 cm−1, respectively. These bands are indicative of disordered defects and the graphite layer present in the CNTs. A noticeable change is also found in the WO3@MWCNT (1:5) nanocomposites, indicating a significant interaction between WO3 and MWCNT in the synthesized nanocomposites.
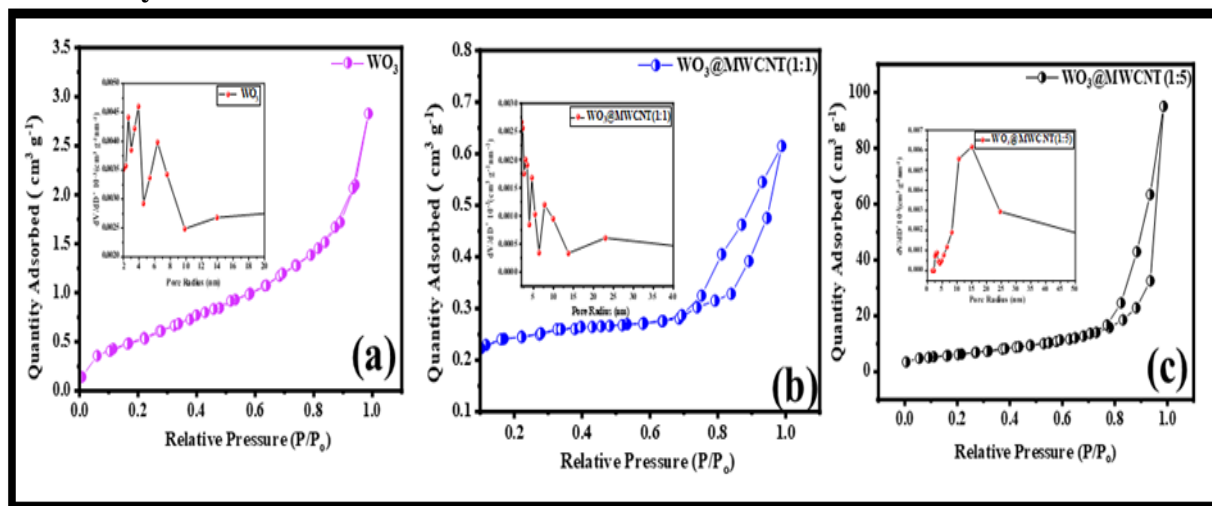
3.5 BET Analysis.

Figure 6 BET analysis (a) pure WO$_3$ (b) WO$_3$@MWCNT (1:1) (c) WO$_3$@MWCNT (1:5) nanocomposites

Figure 6(a-c) demonstrates the utilization of N2 adsorption-desorption measurements pore architectures of the pure WO3 and WO3@MWCNT(1:1) and WO3@MWCNT(1:5) hybrids. Figure 6(a) exhibits conventional type IV hysteresis based on the IUPAC classification. At relative pressures less than 0.65 bar, there is essentially no N2 adsorption on the WO3 sample. In contrast, the N2 adsorption quantity of the WO3@MWCNT (1:5) hybrid increases slowly and is significantly greater than that of pure WO3. WO3 and WO3@MWCNT(1:1) and WO3@MWCNT(1:5) samples have BET-specific surface areas of 24.84, 33and 64.24 m2 g-1, respectively. In addition, Figure 6(b-c) illustrates the BJH-measured pore sizeof pure WO3 and WO3@MWCNT(1:1) and WO3@MWCNT(1:5) hybrid. The average BJH pore volumes of pure WO3 and the hybrid WO3@MWCNT(1:1) and WO3@MWCNT(1:5) are 0.117,0.234 and 0.372 cm3 g−1, respectively. Figure 5(f) shows that the WO3@MWCNT(1:5) hybrid has a broad range of pore sizes, with pores ranging from 2 to 100 nm in radius. The MWCNT-WO3 hybrid, resulting from the synergistic interaction between MWCNTs and WO3 nanorods, exhibits a significantly larger specific surface area and a more homogeneous distribution of pore sizes compared to the pure WO3 nanorods. The MWCNT-WO3 hybrid possesses a large surface area, resulting in an increased number of electrochemically active sites during electrochemical processes. Furthermore, the significant pore volume, when compared to pure WO3, allows for easier entry of electrolyte ions into the inner part of the active substance, leading to improved electrochemical performance [31-34].
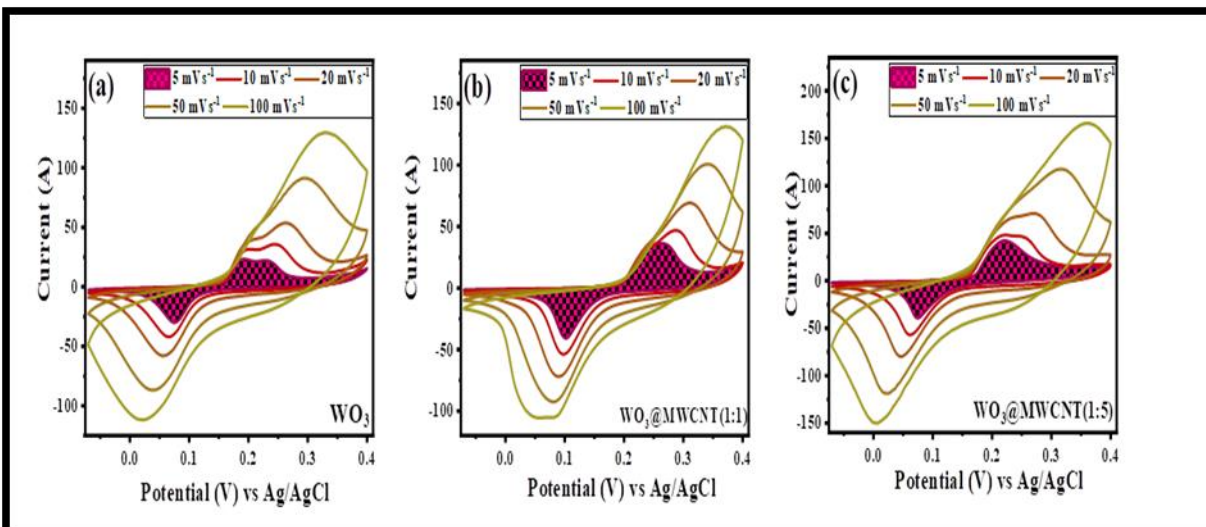
3.6 Electrochemical Performance.

Figure 7 CV analysis at varying scan rate from 5 mVs^{1}to 100 mVs^{-1} (a) pure WO$_3$ (b) WO$_3$@MWCNT (1:1) (c) WO$_3$@MWCNT (1:5)

The first section of Figure 7 displays the cyclic voltammetry (CV) curves of WO3, WO3@MWCNT(1:1), and WO3@MWCNT(1:5) hybrid electrodes. The measurements were taken at 100 mV s–1. The CV curves exhibit a nearly rectangular shape devoid of any discernible redox peaks, indicating that the artificially generated electrodes exhibit exceptional supercapacitive efficiency[35].In addition, the WO3@MWCNT (1:5) hybrid electrode demonstrates better performance. This can be due to its larger volume,and its better anodic and cathodic current responses within the same potential range as the WO3@MWCNT (1:1) and pure WO3 electrodes.The WO3@MWCNT (1:5) hybrid electrode has improved electron transport and a nanorod structure. The discharge times of the electrodes exhibit a consistent trend that aligns with the outcomes of the CV measurements: WO3@MWCNT(1:5) demonstrates the highest discharge time, followed by WO3@MWCNT(1:1), and finally WO3. The WO3@MWCNT(1:5) electrode exhibits excellent electrochemical performance due to the presence of numerous active sites resulting from the combined effect between WO3 spheres and MWCNTs. While the initial discharge curves show a slight decrease in voltage due to internal resistance (IR), the measured IR drop for the WO3@MWCNT(1:5) hybrid is considerably lower than that of the pure WO3 electrode.

Crucially, LiClO4 was employed as the electrolyte, rather than H2SO4, for assessing the electrochemical performance in the current scenario. The CV profiles of the pure WO3, WO3@MWCNT(1:1), and WO3@MWCNT(1:5) hybrid electrodes demonstrate excellent supercapacitive properties, indicating an increased capacity for charge storage in the LiClO4 electrolyte. Moreover, the research suggests that the gel electrolyte has superior stability and durability in comparison to other electrolytes [36]. WO3 demonstrates reversible charge storage due to the change of tungsten from an oxidation state of +5 to +6. It's interesting that storing charge on the WO3@MWCNT(1:5) hybrid electrode didn't change how the supercapacitor worked. This means that the hybrid's structure stayed stable in a neutral solution.
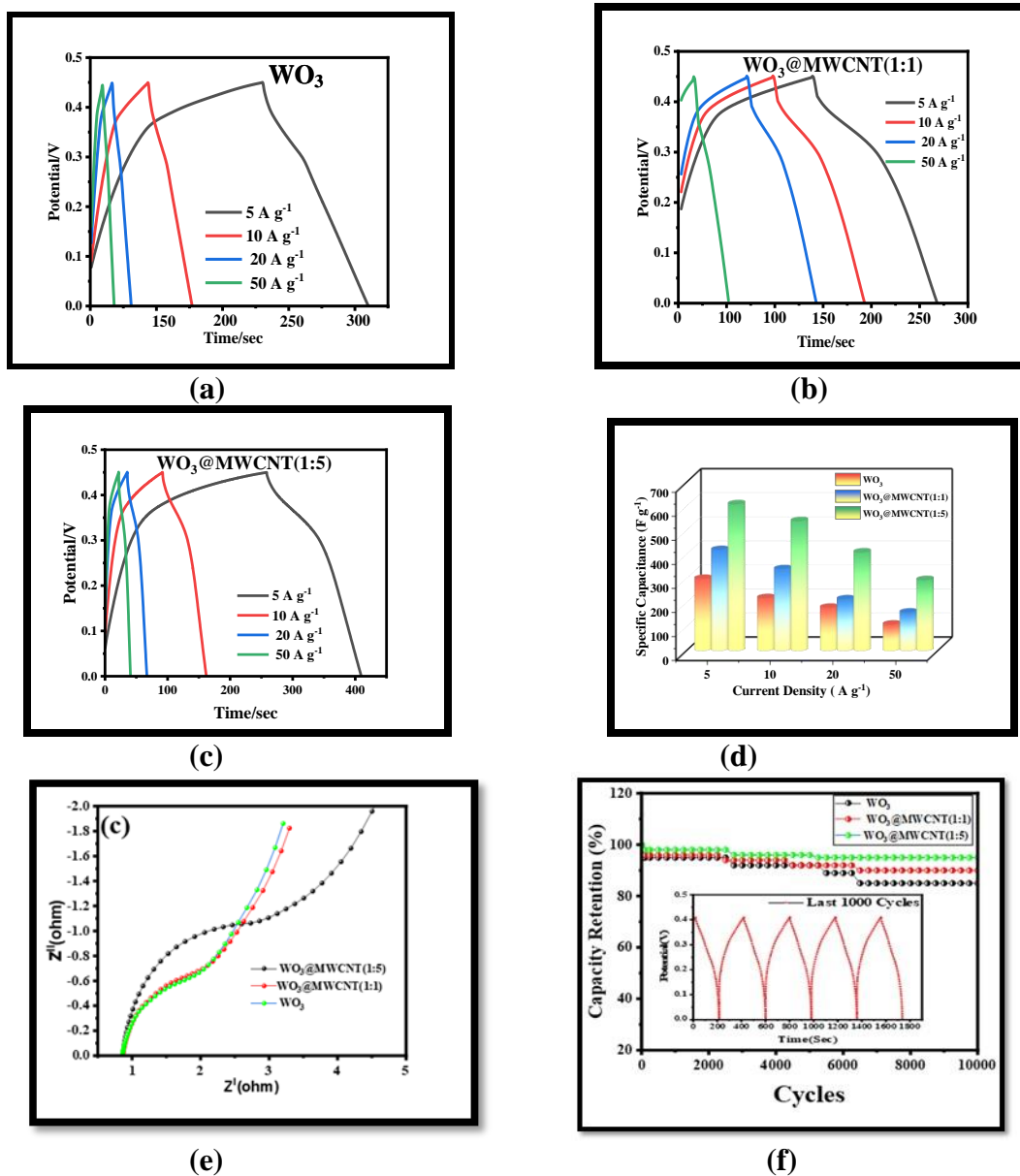
Research Paper
Impact Factor: 7.352
Peer Reviewed Monthly Journal
www.ijmdrr.com

IJMDRR
E- ISSN –2395-1885
ISSN -2395-1877

(a)

(b)

(c)

(d)

(e)

(f)

Figure 8 (a-f) CV , EIS and GCD analysis of pure WO₃, WO₃@MWCNT (1:1) and WO₃@MWCNT (1:5)

Figure 8(a-b) illustrates the GCD curves of the pure WO3, WO3@MWCNT(1:1), and WO3@MWCNT (1:5) hybrid electrodes. These curves were obtained at 5 to 50 Ag^{-1} while maintaining the same operating potential range. The charge-discharge curves exhibit nonlinearity and a low coulombic efficiency.The solid-electrolyte interphase (SEI) layer is formed on the electrode surface when the electrode potential drops below 1 V due to the degradation of the organic electrolyte. The layer exhibits high density, ionic conductivity, and stability. However, when the lithium-ion intercalation/deintercalation occurs during the charge-discharge process, it causes a change in the volume of the electrode, which leads to the compression of the SEI layer [37, 38].

Research Paper
Impact Factor: 7.352
Peer Reviewed Monthly Journal
www.ijmdrr.com

IJMDRR
E- ISSN –2395-1885
ISSN -2395-1877

The electrochemical performance of the prepared electrodes is WO3@MWCNT(1:5) > WO3@MWCNT(1:1) > WO3. The WO3@MWCNT(1:5) hybrid electrode's outstanding electrochemical performance verifies the abundance of active sites caused by the beneficial interaction of WO3 nanorods and MWCNTs. The measured IR drop for the WO3@MWCNT(1:5) is significantly lower than that of the pure WO3 electrode, even if the initial discharge curves reveal a little voltage loss due to resistance (IR drop).

The specific capacitance obtained from the GCD curve is displayed in Figure 8(d). The WO3 coated with MWCNT has a greater capacity in comparison to pure WO3. The specific capacitance of the WO3@MWCNT (1:5) composite material is 610 F g-1 at 5 A g-1, 540 F g-1 at 10 A g-1, 410 F g-1 at 20 A g-1, and 295 F g-1 at 50 A g-1. Conversely, the specific capacitance values for WO3@MWCNT (1:1) are 420, 340, 215, and 160 F g-1, while for WO3 alone they are 330, 220, 180, and 110 F g-1. When comparing the three electrodes, it was found that the WO3@MWCNT (1:5) electrode had the largest capacitance, measuring approximately 610 F g-1. Additionally, this electrode also has a capacity retention of 91%.However, when the lithium-ion intercalation/deintercalation occurs during the charge-discharge process, it causes a change in the volume of the electrode, which leads to the compression of the SEI layer [37, 38]. Furthermore, the observed drop in the infrared (IR) signal suggests that the multi-walled carbon nanotubes (MWCNTs) are actively involved in the electrochemical reactions.

The capacitance diminishes as the current density rises because of the existence of internal active sites that cannot facilitate redox reactions at higher current densities. It presents a comparison of the specific capacitance of the WO3@MWCNT(1:5) with that reported in previous publications. Furthermore, to assess the speed of the chemical reactions and the movement of electric charges in the electrodes that were constructed, Electrochemical Impedance Spectroscopy (EIS) data were gathered at a voltage of 10 mV while no current was flowing, throughout a range of frequencies from 0.01 Hz to 100 kHz. Figure 8(e) displays the Nyquist graphs of the pure WO3, WO3@MWCNT(1:1), and WO3@MWCNT(1:5) electrodes. The Nyquist plot is divided into three basic sections: the high-frequency area, the medium-frequency area, and the low-frequency area. Measurements conducted in the high-frequency range can provide valuable information on the inherent resistance of the active electrode and the interfacial resistance of the substrate to the active material.

In the domain of high frequencies, there is a noticeable impediment to the spread of ions within the active substance, while in the realm of low frequencies, the ions themselves are observed to disperse throughout the substance. Typically, the solution resistance (Rs) and the charge-transfer resistance (Rct) can be determined by analysing the initial intercept point and the extent of the semicircle arc, respectively, on a Nyquist plot in relation to the x-axis. The Nyquist plots indicate that the Rs values for the WO3, WO3@MWCNT(1:1), and WO3@MWCNT(1:5) hybrid electrodes are 2.53 cm-2, 3.24 cm-2, and 3.85 cm-2, respectively. Furthermore, the utilisation of MWCNT, WO3, or WO3@MWCNT(1:5) hybrid electrodes reveals the presence of small semicircular arcs in the high-frequency region. The addition of multi-walled carbon nanotubes (MWCNTs) enhances the electrical conductivity of the WO3@MWCNT(1:5) hybrid electrode, resulting in a lower resistivity (Rs, 0.28 cm -2) compared to pure WO3 (0.285 cm-2).

The supercapacitor's ability to endure repeated cycling is a critical factor in its extensive utilisation. The cycling stabilities of pure WO3 and WO3@MWCNT(1:5) hybrid electrodes were examined by subjecting them to 10,000 repeated CV cycles at a scan rate of 100 m V s-1.

The figure labelled as Figure 8(f) displays the capacity retention values for pure WO3 and WO3@MWCNT(1:5) hybrid electrodes as a function of cycle number. Following 5000 cycles, the original WO3 and WO3@MWCNT(1:5) hybrid electrodes maintained 84.9% and 94.3% of their initial capacities, respectively. Compared to pure tungsten trioxide, the hybrid electrode made of multi-walled carbon nanotubes (MWCNT) and tungsten trioxide (WO3) has better specific capacity and cycle performance. The active material enters a stable state after the first few cycles, during which its specific capacitance decreases. This state lasts for up to 5000 cycles.

The first decrease in specific capacitance observed during cycling can be attributed to the electrochemical activity of the active material. Metal oxides require an activation phase where electrolyte ions circulate constantly within the active ingredient, fully wetting the substance. Due to the limited extent of electrochemical reactions occurring solely on the surface of the electrode, the specific capacitance experiences a drop. Because there are many electrochemically active spots in the material, it can be used up to 5000 times without breaking. The WO3@MWCNT(1:5) hybrid electrode has great electrical conductivity and reaction rates, which made it easy for the tungsten species to move to a higher oxidation state. So, with each turn, the electrode's specific capacity went up.

The WO3@MWCNT(1:5) hybrid electrode demonstrates excellent potential for utilization in a supercapacitor due to its improved specific capacitance, and cyclic stability, as indicated by these data. The electrochemical performance was greatly improved as a result of the combined effect of the interconnected MWCNT nanowires and WO3 nanorods, which utilized both the EDLCs and pseudocapacitance for storing charge. Furthermore, the presence of gaps between the nanowires and nanorods facilitated the entry of electrolyte ions, resulting in a reduction in the distance over which the ions diffused. This, in turn, led to an increase in the lifespan of the electrode when subjected to repeated cycling.

The MWCNTs were also very important in electrochemical processes because they had a lot of surface area, were very strong mechanically, helped keep the nanostructure stable, and made it easier for charges to move between the electrode and solution. Additionally, the resistance was greatly reduced, and the contact between the active material and the current collector got better after a binder-free electrode was made.

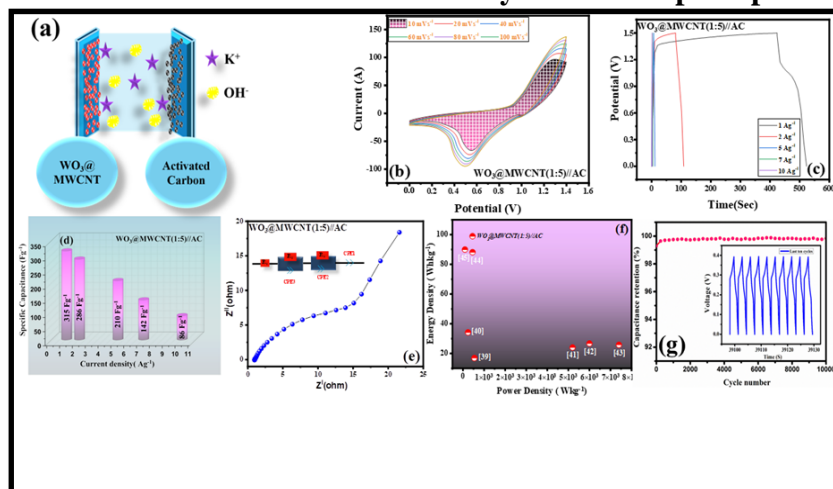### 3.7 Electrochemical Behaviour of Asymmetric Supercapacitor.

Figure 9 (a-e) CV , EIS and GCD analysis of AC//WO$_3$@MWCNT (1:5)

The carbon materials and WO3@MWCNT(1:5) were chosen for the positive and negative electrodes of a novel asymmetric supercapacitor (ASC) based on their electrode properties. Since the voltage of a cell is simply the difference between its positive and negative electrodes, ASCs can have a voltage of up to 1.65 V. The best voltage range for keeping the two-electrode cell stable was found to be between 0 and 1.6 V (Fig. 9b) in the ASC (AC// WO3@MWCNT(1:5)) working unit. The CV curves of the AC// WO3@MWCNT (1:5) ASC device shown in Figure 9b exhibit distorted semi-rectangular-shaped curves with two pairs of redox peaks at an operating voltage of 1.6 V, even at a scan rate of 100 mV s1. This indicates a faradaic pseudocapacitance charge/discharge rate process throughout the entire voltammetric cycle and an excellent fast charge/discharge performance. Ions diffuse more efficiently into the active sites at slower scan rates. Higher scan rates reduce the depth to which the ions can penetrate a substance. Electrode supercapacitors show high-rate capabilities because the active site interacts with ions more effectively at slower scanning rates. High symmetry in the GCD curves (Fig. 9c) indicates good capacitive performance and electrochemical reversibility in AC// WO3@MWCNT(1:5) ASC at various current densities. The calculated specific capacitance is about 315 F g^{-1} at 10 A g^{-1}.

EIS tests were performed across the frequency range of 0.1 Hz to 100 kHz on the AC// WO3@MWCNT(1:5) ASC to better investigate its ion transport capabilities (Fig. 9d). At low frequencies, the Nyquist plot displays a linear section, suggesting a strong capacitive behaviour; at high frequencies, it narrows down to a semicircle, indicating a low charge transfer resistance. By incorporating the electrolyte's bulk resistance, the electrode's contact resistance, and the electroactive materials' intrinsic resistance, the equivalent series resistance (Rs) can be calculated from the EIS data plotted on the real axis (refer to the inset of Figure 9d).The presence of Rct at the electrode-electrolyte interface is a result of the interaction between a faradaic and electronic double-layer capacitor (Cdl). The frequency dependence of ion diffusion/transport in electrolytes results in the Warburg impedance (ZW), a 45-degree sloping curve at intermediate frequencies. Figure 9d indicates that the AC// WO3@MWCNT(1:5) electrode has a low Rct (0.68 U) and a low Rs (0.813 U), indicating that the charge is transferred quickly in ASC.

Using the GCD data, the Ragone plot of the AC// WO3@MWCNT(1:5)ASC device is calculated (shown in Fig. 8e). At a power density of 631 W kg1, the AC// WO3@MWCNT(1:5) ASC clearly displays an energy density of 25.3 W h kg1, while at a power density of 8529.4 W kg1, the energy density is still maintained at 13.2 W h kg1. As shown in Fig. 9e, the AC// WO3@MWCNT(1:5)ASC has a significantly greater maximum energy density than both the symmetrical and asymmetrical supercapacitors used in the prior work.

Supercapacitors rely heavily on cycling stability. GCD cycling at a current density of 0.5 – 10 Ag^{-1} was used to analyze the AC// WO3@MWCNT(1:5)ASC's long-term stability (Fig. 9f). The electrode material was unstable for the first 2000 cycles, but after 5000 cycles, the ASC's specific capacitance remains at 82.6%, demonstrating its superior electrochemical stability. Due to its remarkable durability in repeated cycles, which may be attributed to the porous carbon material and the exceptional electrochemical performance of AC// WO3@MWCNT(1:5) during the process of charging and discharging, this material is a viable choice for long-term energy storage devices.

Conclusion

The hydrothermal procedure greatly influences the form, crystallinity, and electrochemical properties of WO3@MWCNT(1:5) during the hydrothermal reaction. The WO3@MWCNT(1:5) composite material exhibits the maximum specific capacitance of 610 Fg-1 at 0.5 A g1. Additionally, this material possesses a regular hexagonal form. A simple and cost-effective method was used to produce porous-activated carbon.The WO3@MWCNT(1:5) material, which has a porous structure in three dimensions, exhibits a high specific capacitance and exceptional cycling stability, retaining 96% of its initial specific capacitance after 5000 cycles. An aqueous asymmetric supercapacitor (ASC) was constructed using a stable hexagonal-like WO3@MWCNT(1:5) as the positive electrode and activated carbon (AC) as the negative electrode, resulting in a high-energy-density configuration. The fully assembled ASC exhibited remarkable durability, retaining 82.6% of its original specific capacitance after 10,000 cycles. Additionally, it achieved a substantial energy density of 25.3 W h kg1 at a power density of 631.1 W kg1, while maintaining an output voltage of 0.5 V. The synthesis process employed in this work offers a novel approach for producing alkali metal tungsten trioxide, which can be used for energy storage purposes.

References

1. N. Choudhary, C. Li, J. Moore, N. Nagaiah, L. Zhai, Y. Jung and J. Thomas, Supercapacitors: Asymmetric Supercapacitor Electrodes and Devices, Adv. Mater., 2017, 29, 1605336.
2. M. Gidwani, A. Bhagwani and N. Rohra, Supercapacitors: the near future of batteries, Int. J. Eng. Inventions, 2014, 4, 22–27.
3. B. Scrosati, J. Hassoun and Y. K. Sun, Lithium-ion batteries. A look into the future, Energy Environ. Sci., 2011, 4, 3287– 3295.
4. C. Liu, F. Li, L.-P. Ma and H. M. Cheng, Advanced materials for energy storage, Adv. Mater., 2010, 22, 28.
5. M. Winter and R. J. Brodd, What are batteries, fuel cells, and supercapacitors, Chem. Rev., 2004, 104, 4245–4270.
6. B. E. Conway, Electrochemical Supercapacitors: Scientific Fundamentals, Technological Applications, Springer Sci. Business Media, 2013.
7. Z. L. Wang, Piezopotential Gated Nanowire Devices: Piezotronics and Piezo-Phototronics, Nano Today, 2010, 5, 540–552.
8. P. Simon and Y. Gogotsi, Materials for Electrochemical Capacitors, Nat. Mater., 2008, 7, 845–854.
9. J. Kondoh, I. Ishii, H. Yamaguchi, A. Murata, K. Otani, K. Sakuta, N. Higuchi, S. Sekine and M. Kamimoto, Electrical energy storage systems for energy networks, Energy Convers. Manage., 2000, 41, 1863–1874.
10. V. Augustyn, P. Simon and B. Dunn, Pseudocapacitive oxide materials for high-rate electrochemical energy storage, Energy Environ. Sci., 2014, 7, 1597–1614.
11. P. C. Chen, G. Shen, Y. Shi, H. Chen and C. Zhou, Preparation and characterization of flexible asymmetric supercapacitors based on transition-metal-oxide nanowire/ single-walled carbon nanotube hybrid thin-film electrodes, ACS Nano, 2010, 4, 4403–4411.
12. S. K. Balasingam, J. S. Lee and Y. Jun, Few-layered MoSe2 nanosheets as an advanced electrode material for supercapacitors, Dalton Trans., 2015, 44, 15491–15498.
13. H. Pang, X. Li, Q. Zhao, H. Xue, W. Y. Lai, Z. Hu and W. Huang, One-pot synthesis of heterogeneous Co3O4- nanocube/Co(OH)2-nanosheet hybrids for high-performance flexible asymmetric all-solid-state supercapacitors, Nano Energy, 2017, 35, 138–145.

14. M. A. Borysiewicz, M. Ekielski, Z. Ogorzałek, M. Wzorek, J. Kaczmarski and T. Wojciechowski, Highly transparent supercapacitors based on ZnO/MnO2 nanostructures, Nanoscale, 2017, 9, 7577–7587.

15. X. Lu, T. Zhai, X. Zhang, Y. Shen, L. Yuan, B. Hu, L. Gong, J. Chen, Y. Gao, J. Zhou, Y. Tong and Z. L. Wang, WO3- x@Au@MnO2 core–shell nanowires on carbon fabric for high-performance flexible supercapacitors, Adv. Mater., 2012, 24, 938–944.

16. C. Jo, J. Wang, H. Song, A. H. Dao, Y.-T. Kim, S. H. Lee, S. W. Hong, S. Yoon and J. Lee, Capacitors: Block Copolymer Assisted One Pot Synthesis of Ordered Mesoporous WO3-x/Carbon Nanocomposites as High-Rate Performance Electrodes for Pseudocapacitors, Adv. Funct. Mater., 2013, 23, 3713.

17. W. Su, L. Zhou and Y. P. Zhou, Preparation of microporous activated carbon from coconut shells without activating agents, Carbon, 2003, 41, 861–863.

18. G. Ma, F. Hua, K. Sun, Z. Zhang, E. Feng, H. Peng and Z. Lei, Porous carbon derived from sorghum stalk for symmetric supercapacitor, RSC Adv., 2016, 6, 103508–103516.

19. F. Gao, J. Qu, Z. Zhao, Z. Wang and J. Qiu, Nitrogen-doped activated carbon derived from prawn shells for high-performance supercapacitors, Electrochim. Acta, 2016, 190, 1134–1141.

20. L. Sun, C. Tian, M. Li, X. Meng, L. Wang, R. Wang, J. Yin and H. Fu, From coconut shell to porous graphene-like nanosheets for high-power supercapacitors, J. Mater. Chem. A, 2013, 1, 6462–6470.

21. C. Long, X. Chen, L. Jiang, L. Zhi and Z. Fan, Porous layer stacking carbon derived from in-built template in biomass for high volumetric performance supercapacitors, Nano Energy, 2015, 12, 141–151.

22. A. Burke, Ultracapacitors: why, how, and where is the technology, J. Power Sources, 2000, 91, 37–50.

23. P. J. Hall and E. J. Bain, Energy-storage technologies and electricity generation, Energy Policy, 2008, 36, 4352–4355.

24. I. Hadjipaschalis, A. Poullikkas and V. Efthimiou, Overview of current and future energy storage technologies for electric power applications, Renew. Sustain. Energy Rev., 2009, 13, 1513–1522.

25. Y. Zhao, L. Hu, S. Zhao and L. Wu, Preparation of MnCo2O4@Ni(OH)2 Core–Shell Flowers for Asymmetric Supercapacitor Materials with Ultrahigh Specific Capacitance, Adv. Funct. Mater., 2016, 26, 4085–4093. 26 R. D. Kumar, Y. Andou and S. Karuppuchamy, Facile synthesis of Co–WO3/functionalized carbon nanotube nanocomposites for supercapacitor applications, J. Mater. Sci. Mater. Electron., 2017, 28, 5425–5434.

26. M. Qiu, P. Sun, L. Shen, K. Wang, S. Song, X. Yu, S. Tan, C. Zhao and W. Mai, WO3 nano flowers with excellent pseudo-capacitive performance and the capacitance contribution analysis, J. Mater. Chem. A, 2016, 4, 7266–7273.

27. Z. Pan, Y. Qiu, J. Yang, F. Ye, Y. Xu, X. Zhang, M. Liu and Y. Zhang, Ultra-endurance flexible all-solid-state asymmetric supercapacitors based on three-dimensionally coated MnOx nanosheets on nanoporous current collectors, Nano Energy, 2016, 26, 610–619.

28. X. Tang, Y. Lui, A. Merhi, B. Chen, S. Ding, B. Zhang and S. Hu, Redox-active hydrogel polymer electrolytes with different pH values for enhancing the energy density of the hybrid solid-state supercapacitor, ACS Appl. Mater. Interfaces, 2017, 9, 44429–44440.

29. G. Cai, J. Tu, D. Zhou, L. Li, J. Zhang, X. Wang and C. Gu, The direct growth of a WO3 nanosheet array on a transparent conducting substrate for highly efficient electrochromic and electrocatalytic applications, Crystengcomm, 2014, 16, 6866–6872.

30. J. Wang, E. Khoo, P. S. Lee and J. Ma, Synthesis, Assembly, and Electrochromic Properties of Uniform Crystalline WO3 Nanorods, J. Phys. Chem. C, 2008, 112, 14306–14312.

31. C. Navio, S. Vallejos, T. Stoycheva, E. Llobet, X. Correig, R. Snyders, C. Blackman, P. Umek, X. Ke, G. V. Tendeloo and C. Bittencourt, Gold clusters on WO3 nanoneedles grown via AACVD: XPS and TEM studies, Mater. Chem. Phys., 2012, 134, 809–813.

32. P. A. Shinde, A. C. Lokhande, N. R. Chodankar, A. M. Patil, J. H. Kim and C. D. Lokhande, Temperature-dependent surface morphological modifications of hexagonal WO3 thin films for high-performance supercapacitor application, Electrochim. Acta, 2017, 224, 397–404.

33. A. Y. Gokhshtein, PoverkhnostnoeNatyazhenieTverdykh Tel I Adsorbtsiya (The Surface Stress in Solids and the Adsorption), Nauka Moscow (in Russian), 1976.

34. Z. Fan, J. Yan, T. Wei, L. Zhi, G. Ning, T. Li and F. Wei, Asymmetric Supercapacitors Based on Graphene/MnO2 and Activated Carbon Nanofiber Electrodes with High Power and Energy Density, Adv. Funct. Mater., 2011, 21, 2366–2375.

35. S. Gao, K. Geng, H. Liu, X. Wei, M. Zhang, P. Wang and J. Wang, Transforming organic-rich amaranthus waste into nitrogen-doped carbon with superior performance of the oxygen reduction reaction, Energy Environ. Sci., 2015, 8, 221–229.

36. A. Sadezky, H. Muckenhuber, H. Grothe, R. Niessner and U. P˙oschl, Raman microspectroscopy of soot and related carbonaceous materials: spectral analysis and structural information, Carbon, 2005, 43, 1731–1742.

37. H. Wang, Z. Xu, A. Kohandehghan, Z. Li, K. Cui, X. Tan, T. J. Stephenson, C. K. King'ondu, C. M. Holt, B. C. Olsen, J. K. Tak, D. Harfield, A. O. Anyia and D. Mitlin, Interconnected carbon nanosheets derived from hemp for ultrafast supercapacitors with high energy, ACS Nano, 2013, 7, 5131–5141.